Site-selective insulating phase in a twisted bilayer Hubbard model

Xiu-Cai Jiang, Ze Ruan, and Yu-Zhong Zhang[*]

Shanghai Key Laboratory of Special Artificial Microstructure Materials and Technology, School of Physics Science and Engineering, Tongji University, Shanghai 200092, People's Republic of China

The paramagnetic phase diagrams of the half-filled Hubbard model on a twisted bilayer square lattice are investigated using the coherent potential approximation. In addition to the conventional metallic, band insulating, and Mott insulating phases, we find two site-selective insulating phases where certain sites exhibit band insulating behaviors while the others display Mott insulating behaviors. These phases are identified by the band gap, the double occupancy, the density of states, as well as the imaginary part of the self-energy. Furthermore, we examine the effect of on-site potential on the stability of the site-selective insulating phases. Our results indicate that fruitful site-selective phases can be engineered by twisting.

I. INTRODUCTION

Layered systems with twists have recently attracted a great deal of attention due to the discovery of numerous fascinating quantum phases, such as the Mott insulator [1–5], superconductivity [6,7], and topological phases [8–10]. Meanwhile, the Hubbard model, employed to study various intriguing phases including the Mott insulator [11], the orbital-selective phase [12–15], the bond-ordered insulator [16,17], superconductivity [18,19], antiferromagnetism [20–22], etc., has received significant interest for decades. Therefore, introducing twists in the Hubbard model may induce novel phases, which are currently hot topics. Until now, much effort has been spent on the Hubbard model describing twisted transition-metal dichalcogenides [23–27] or twisted bilayer graphene [28], predicting numbers of correlated phases. In addition, a few works investigate the Hubbard model on twisted bilayer square lattices, but they focus primarily on superconducting phase transitions [29,30]. However, the phase transitions among Mott insulators, band insulators, and metal in the Hubbard model on a twisted bilayer square lattice remain unexplored.

As we know, even for the untwisted bilayer Hubbard model, the phase transitions at half filling are fascinating and have been widely investigated. Such a model can not only describe high-temperature cuprate superconductors [31], but it can also be experimentally realized through fermionic atoms trapped in an optical lattice [32]. Quantum Monte Carlo simulations have revealed that the interlayer hopping suppresses intralayer long-range magnetic order in such a model on the square lattice [33]. Applying dynamical mean-field theory to the bilayer Hubbard model on a Bethe lattice, a smooth crossover between band and Mott insulators is discovered within the paramagnetic phase diagram [34]. Furthermore, the magnetic phase diagram of this model on a square

lattice is explored by cluster dynamical mean-field theory [35] and quantum Monte Carlo simulations [36,37], where strong on-site Coulomb interaction localizes electrons with weak interlayer hopping, favoring a Mott insulator, while strong interlayer hopping opens a gap between the bonding and antibonding bands, resulting in a band insulator. Although these works [35–37] also suggest a paramagnetic metallic phase in the magnetic phase diagram when both on-site Coulomb interaction and interlayer hopping are weak, further investigations clarify it as an antiferromagnetic insulating phase due to the perfect nesting property of the Fermi surface within the noninteracting system [38,39]. In contrast, a metallic phase can appear in the paramagnetic phase diagram with weak on-site Coulomb interaction present [39]. In addition to these findings, superconductivity [40–46], non-Fermi-liquid [47], density-ordered and superfluid phases [48] have also been reported in the bilayer Hubbard model or its extended versions as doping away from half-filling.

When the twist is applied to the layered systems, the well-known moiré pattern emerges, giving rise to distinct hoppings present at the inequivalent sublattices due to different atomic environments. In fact, distinct hoppings on different sublattices may cause a site-selective phase. A typical example is that bond-length disproportionation, corresponding to inequivalent sublattices having distinct hoppings, leads to a site-selective insulating phase in RNiO$_3$ (R = Sm, Eu, Y, or Lu), where certain Ni atoms exhibit a magnetic Mott insulating state while the remaining Ni atoms form a singlet insulating state [49]. Moreover, site-selective magnetic phases have also been reported in other materials with inequivalent sublattices [50,51]. Given that the interlayer hoppings favor a band insulator in a bilayer square lattice, the instabilities of the band insulating state against the Mott insulator on inequivalent sublattices of a twisted bilayer square lattice may be different in the presence of a strong on-site Coulomb interaction due to distinct interlayer hoppings. Therefore, a site-selective insulating phase is likely to appear in such a twisted system, characterized by some sites entering a Mott
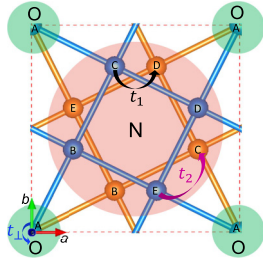
*Corresponding author: yzzhang@tongji.edu.cn

FIG. 1. The structure of a bilayer square lattice (top view) with a twisted angle of $\theta = 53.13°$, where different interlayer hoppings are also shown, including interlayer nearest-neighbor hopping $t_\perp$, interlayer next-nearest-neighbor hopping t_1, and interlayer third-nearest-neighbor hopping t_2. There are two types of inequivalent sites within the supercell, containing two overlapping sites and eight nonoverlapping sites (as viewed from the top), which are located in region O (green) and region N (light orange), respectively.

insulating state while others remain in a band insulating state.

In this paper, we aim to point out the presence of site-selective insulating phases in the half-filled Hubbard model on a twisted bilayer square lattice. To this end, taking the case with a twisted angle of $\theta = 53.13°$ as an example, we investigate the paramagnetic phase diagrams of this model under the combined effect of on-site Coulomb interaction and various interlayer hoppings using the coherent potential approximation (CPA). Interestingly, we obtain two site-selective insulating phases, where certain sites exhibit band insulating states while the rest display Mott insulating states, when one type of interlayer hopping is strong while the remaining interlayer hoppings are weak if the strong on-site Coulomb interaction is involved. In addition, we also discover Mott insulating, band insulating, and metallic phases in this model, which have been observed in the untwisted bilayer Hubbard model as well. The Mott insulating phase emerges when strong on-site Coulomb interaction wins over all the weak interlayer hoppings. In contrast, strong $t_\perp$, either in cooperation with strong t_1 or strong t_2, favors the band insulating phase (the definitions of $t_\perp$, t_1, and t_2 can be found in Fig. 1). Furthermore, we have illustrated that the site-selective insulating phases are stable even in the presence of a moderate site-dependent on-site potential. Our findings not only demonstrate a fascinating phenomenon that the band insulating state and Mott insulating state can coexist in twisted strongly correlated systems, but they also suggest twist as an effective approach to access a site-selective phase.

The rest of this paper is organized as follows: Section II describes the details of the structure, the model, and the method we used. Section III demonstrates our primary results, including the paramagnetic phase diagrams under different parameters, the gaps and double occupancies as functions of various interlayer hoppings, the density of states (DOS), the imaginary part of the self-energy, the DOS at the Fermi level varied with the Lorentzian broadening factor, as well as the effect of an on-site potential difference on the stability of the site-selective phases. Section IV includes a discussion of our results, and Sec. V concludes with a summary.

II. MODEL AND METHOD

To demonstrate the presence of site-selective insulating phases in the half-filled Hubbard model on a twisted bilayer square lattice, we take the case with a twisted angle of $\theta = 53.13°$ as an example since it is the smallest commensurate structure of a twisted bilayer square lattice as presented in Fig. 1, which has also been used to study the superconducting phase transitions [29]. According to the atomic environment, two types of inequivalent sites are distinguished within the supercell, containing two overlapping sites and eight nonoverlapping sites (as viewed from the top), which are located at region O (green) and region N (light orange), respectively. Then, the Hamiltonian can be written as

$$H = H_k + H_\perp + H_\Delta + H_\mu + H_U \tag{1}$$

with

$$H_k = -t_0 \sum_{m\sigma} \sum_{\langle is, js' \rangle} C^\dagger_{ism\sigma} C_{js'm\sigma},$$

$$H_\perp = -t_\perp \sum_{i\sigma} (C^\dagger_{iA1\sigma} C_{iA2\sigma} + \text{H.c.})$$

$$- t_1 \sum_{i\sigma} \sum_{\langle\langle s,s'\rangle\rangle} (C^\dagger_{is1\sigma} C_{is'2\sigma} + \text{H.c.})$$

$$- t_2 \sum_{i\sigma} \sum_{\langle\langle\langle s,s'\rangle\rangle\rangle} (C^\dagger_{is1\sigma} C_{is'2\sigma} + \text{H.c.}),$$

$$H_\Delta = \Delta_O \sum_{im\sigma} n_{iAm\sigma} + \Delta_N \sum_{im\sigma} \sum_{s\in N} n_{ism\sigma},$$

$$H_\mu = -\mu \sum_{ism\sigma} n_{ism\sigma},$$

$$H_U = U \sum_{ism} n_{ism\uparrow} n_{ism\downarrow}, \tag{2}$$

where H_k is the Hamiltonian of the intralayer nearest-neighbor hopping. $H_\perp$ is the Hamiltonian describing interlayer nearest-neighbor, next-nearest-neighbor, and third-nearest-neighbor hoppings. H_Δ and H_μ denote separately the energies of the on-site potential and the chemical potential. H_U depicts the on-site Coulomb repulsive interaction between spin-up and spin-down electrons. Here, $i(j)$, $s(s')$, m, and σ denote separately the cell, sublattice, layer, and spin indexes. $\langle is, js' \rangle$, $\langle\langle s, s' \rangle\rangle$, and $\langle\langle\langle s, s' \rangle\rangle\rangle$ stand for the summations over the intralayer nearest-neighbor sites, interlayer next-nearest-neighbor sites, and interlayer third-nearest-neighbor sites, respectively. t_0 and $t_\perp (t_1, t_2)$ represent individually the intralayer nearest-neighbor hopping integral and the interlayer nearest (next-nearest, third-nearest)-neighbor hopping integral. Δ_O and Δ_N are on-site potentials of the inequivalent sublattices. μ is the chemical potential, and U is the on-site Coulomb repulsive interaction.

We now introduce how to employ the CPA to solve this many-body Hamiltonian. Hubbard views the electron correlation problem as a disordered alloy where an electron with spin σ moving in the system encounters either a potential of U at a site with a spin $\bar{\sigma}$ present or 0 without [52]. Then, the alloy

analogy of this Hubbard model has the following form:

$$H_A = H_k + H_\perp + H_\Delta + H_\mu + \sum_{ism\sigma} E_{ism\sigma} n_{ism\sigma}, \qquad (3)$$

where $E_{ism\sigma}$ is a disordered potential depending on the presence of a spin $\bar{\sigma}$. Specifically, $E_{ism\sigma} = U$ with a probability of $P_U = \langle n_{ism\bar{\sigma}} \rangle$ or $E_{ism\sigma} = 0$ with a probability of $P_0 = 1 - \langle n_{ism\bar{\sigma}} \rangle$. The Green's function of this disordered model necessitates the computation of an average over all possible disordered configurations. However, performing this calculation exactly is impossible, and the CPA should be employed to solve this alloy problem [53–55]. Within the framework of the CPA, the disordered alloy is self-consistently mapped into an effective medium, i.e., the disordered potential $E_{ism\sigma}$ is substituted with an energy-dependent, site-diagonal, and translationally invariant self-energy $\Sigma_{sm\sigma}$. Then, the Hamiltonian of the effective medium within the CPA becomes

$$H_{\text{eff}} = H_k + H_\perp + H_\Delta + H_\mu + \sum_{ism\sigma} \Sigma_{sm\sigma} n_{ism\sigma}. \qquad (4)$$

The detailed mapping from model (3) to model (4) is given in Appendix. Noticeably, despite some inherent limitations [56], the CPA remains valuable as a reliable and computationally cheap method for capturing the phase transitions among a band insulator, metal, and Mott insulator in many-body systems. For example, the CPA successfully reproduces the phase diagram of the ionic Hubbard model at half-filling [57,58], the critical on-site Coulomb interaction for the Mott transition on the honeycomb lattice at half-filling obtained by the CPA [59] is consistent with the results of the quantum Monte Carlo simulations [60–62] and cluster dynamical mean-field theory [63,64], and the experimental discrepancies of the gap in both bilayer graphene [65,66] and graphene/h-BN heterostructure [67,68] have been successfully understood by employing the CPA to investigate their phase diagrams [69,70].

III. RESULTS

Now, we will demonstrate the presence of site-selective insulating phases in the paramagnetic phase diagrams of the half-filled Hubbard model on this twisted bilayer square lattice. To this end, we employ the CPA to calculate the paramagnetic phase diagrams of this model under the combined effect of on-site Coulomb interaction and various interlayer hoppings, where three interlayer hoppings are concerned, including interlayer nearest-neighbor hopping $t_\perp$, interlayer next-nearest-neighbor hopping t_1, and interlayer third-nearest-neighbor hopping t_2. Figure 2(a) illustrates the phase diagram in the U/t_0-$t_\perp/t_0$ plane at $t_1/t_0 = t_2/t_0 = 0$. As can be seen, when interlayer hoppings are absent, equivalent to two unrelated monolayer square lattices, the system undergoes a phase transition from metal to Mott insulator with increasing on-site Coulomb interaction, consistent with the results obtained by other methods [39,71,72]. Thus, the CPA provides reliable results for two irrelevant monolayer square lattices, and we go on with the case of interlayer hoppings present. Remarkably, a site-selective insulating phase (BI+MI), where overlapping sites exhibit a band insulating state while nonoverlapping sites display a Mott insulating state, emerges at the region of strong on-site Coulomb interaction if the interlayer
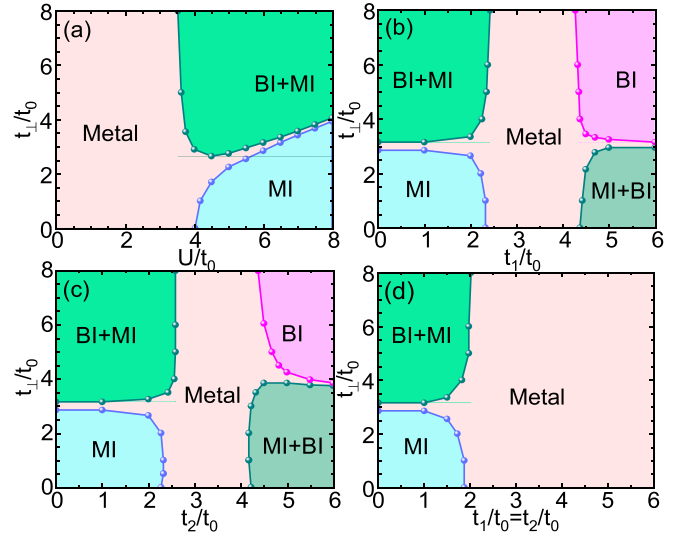

FIG. 2. The paramagnetic phase diagrams of the half-filled Hubbard model on a twisted bilayer square lattice, involing (a) the U/t_0-$t_\perp/t_0$ plane at $t_1/t_0 = t_2/t_0 = 0$, (b) the t_1/t_0-$t_\perp/t_0$ plane when $U = 6t_0$ and $t_2/t_0 = 0$, (c) the t_2/t_0-$t_\perp/t_0$ plane when $U = 6t_0$ and $t_1/t_0 = 0$, and (d) the $(t_1/t_0 = t_2/t_0)$-$t_\perp/t_0$ plane at $U = 6t_0$. t_0 and $t_\perp$ (t_1, t_2) are individually the intralayer and interlayer nearest (next-nearest, third-nearest)-neighbor hopping integrals. BI, MI, and BI+MI (MI+BI) denote the band insulating phase, Mott insulating phase, and site-selective insulating phase, respectively. Noticeably, BI+MI and MI+BI are two distinct site-selective insulating phases. Specifically, BI+MI (MI+BI) describes a site-selective insulating phase where the overlapping sites (located at region O) exhibit a band (Mott) insulating state while the nonoverlapping sites (located at region N) manifest a Mott (band) insulating state.

nearest-neighbor hopping $t_\perp$ exceeds a critical value. This is because a strong $t_\perp$ generates interlayer singlets at the overlapping sites, corresponding to the appearance of a band insulating state there [37,39], while a strong on-site Coulomb interaction U stabilizes a Mott insulator state at nonoverlapping sites due to the lack of interlayer hoppings.

Figures 2(b) and 2(c) demonstrate the phase diagrams in the t_1/t_0-$t_\perp/t_0$ plane at $t_2/t_0 = 0$ and the t_2/t_0-$t_\perp/t_0$ plane at $t_1/t_0 = 0$, respectively, under a strong on-site Coulomb interaction of $U = 6t_0$. Interestingly, two distinct site-selective insulating phases are observed in both phase diagrams, specifically BI+MI and MI+BI, where MI+BI is the counterpart phase of BI+MI. In MI+BI, a Mott (band) insulating state is replaced by a band (Mott) insulating state at specific sites compared with BI+MI. Besides, despite slight differences in the phase boundaries, both phase diagrams contain the same phases. This happens because increasing either t_1 or t_2 will destroy the Mott insulating state at nonoverlapping sites and subsequently form a band insulating state there. Consequently, as either t_1 or t_2 is increased, the system experiences phase transitions from the Mott insulating phase to a metallic phase and then into MI+BI for a weak $t_\perp$ while it evolves from BI+MI to a metallic phase and then into the band insulating phase for a strong $t_\perp$.

The phase diagram in the $(t_1/t_0 = t_2/t_0)$-$t_\perp/t_0$ plane is also investigated when $U = 6t_0$ as illustrated in Fig. 2(d).
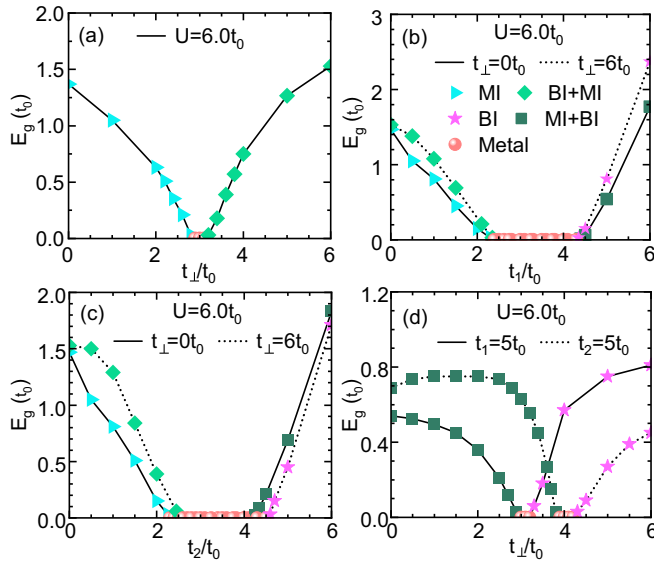
FIG. 3. The band gaps as functions of various interlayer hoppings. (a) The band gap varies with interlayer nearest-neighbor hopping $t_\perp$ when $t_1/t_0 = t_2/t_0 = 0$ and $U = 6t_0$. (b) Band gaps as functions of interlayer next-nearest-neighbor hopping t_1 for two indicated $t_\perp$ values, namely $0t_0$ (solid line) and $6t_0$ (dotted line), where $t_2/t_0 = 0$ and $U = 6t_0$ are used. (c) Band gaps as functions of interlayer third-nearest-neighbor hopping t_2 for two specified $t_\perp$ values, $0t_0$ (solid line) and $6t_0$ (dotted line), where $t_1/t_0 = 0$ and $U = 6t_0$ are adopted. (d) The evolution of band gaps with interlayer nearest-neighbor hopping $t_\perp$ when $t_1 = 5t_0$ and $U = 6t_0$ (solid line) as well as when $t_2 = 5t_0$ and $U = 6t_0$ (dotted line). The green diamonds and malachite green squares represent two distinct site-selective phases. The pink pentagram, cyan triangle, and orange ball denote the band insulating, Mott insulating, and metallic phases, respectively.

Apparently, the enhancement of both t_1 and t_2 also destroys the Mott insulating state at nonoverlapping sites. As a result, although the critical values of t_1 and t_2 resulting in the phase transition decrease, the phase transitions in Fig. 2(d) are comparable to those in Figs. 2(b) and 2(c) when both t_1 and t_2 are weak. However, in the region where both t_1 and t_2 are strong, neither BI nor MI+BI will occur as the interlayer singlets between nonoverlapping sites fail to form when strong t_1 and strong t_2 are present simultaneously. Please note that further increasing t_1 in Fig. 2(b), t_2 in Fig. 2(c), or both t_1 and t_2 in Fig. 2(d) will not induce additional phase transitions.

In brief, in this twisted bilayer Hubbard model, we not only observe the Mott insulating, band insulating, and metallic phases proposed in the untwisted case, but we also identify two site-selective phases with the coexistence of band and Mott insulating states. These findings suggest twist as an effective approach to access a site-selective phase in strongly correlated systems.

Next, we proceed to explain how the phases in the paramagnetic phase diagrams (Fig. 2) are determined. As the trend in the band gap with interlayer hopping provides a valuable distinguishing characteristic for the phases in the untwisted case [35], we plot the evolution of the band gap in this twisted system under various interlayer hoppings in Fig. 3, where a sufficiently strong on-site Coulomb interaction with $U = 6t_0$
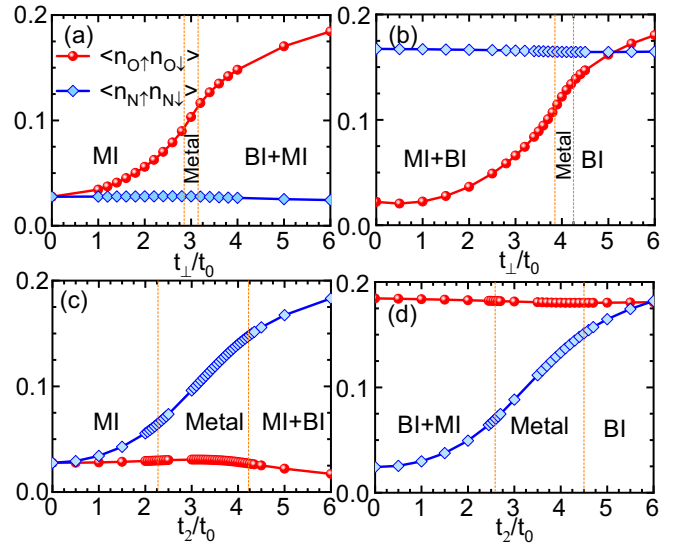

FIG. 4. The double occupancies on different sublattices as functions of various interlayer hoppings. (a) The double occupancies on different sublattices vary with interlayer nearest-neighbor hopping $t_\perp$ when $t_1/t_0 = t_2/t_0 = 0$ and $U = 6t_0$. (b) The double occupancies on different sublattices as functions of $t_\perp$ when $t_2/t_0 = 5$, $t_1/t_0 = 0$, and $U = 6t_0$. (c) The double occupancies on different sublattices vary with interlayer next-nearest-neighbor hopping t_2 when $t_\perp/t_0 = t_1/t_0 = 0$ and $U = 6t_0$. (d) The double occupancies on different sublattices as functions of t_2 when $t_\perp/t_0 = 6$, $t_1/t_0 = 0$, and $U = 6t_0$.

is adopted. We discover that the band gap first closes and then reopens as $t_\perp$ increases in the absence of other interlayer hoppings [Fig. 3(a)], confirming the presence of two insulating phases separated by a metallic phase within the U/t_0-$t_\perp/t_0$ plane [Fig. 2(a)]. By inspecting the effect of t_1 [Fig. 3(b)] and that of t_2 [Fig. 3(c)] on the band gap of these two insulating phases, four insulating phases are distinguishable in both the t_1/t_0-$t_\perp/t_0$ plane [Fig. 2(b)] and the t_2/t_0-$t_\perp/t_0$ plane [Fig. 2(c)]. This can be understood by the following facts: the band gaps of two insulating phases observed in the U/t_0-$t_\perp/t_0$ plane gradually vanish as t_1 or t_2 is increased, indicating their disappearances, meanwhile the gaps reopen and increase for strong values of both t_1 and t_2, implying the occurrence of additional insulating phases which are confirmed by Fig. 3(d) as two new insulating phases.

Besides the behavior of the band gap, we further confirm the presence of four distinct insulating phases by analyzing the double occupancy. Figure 4 demonstrates the evolutions of double occupancies on inequivalent sites as functions of t_2 ($t_\perp$) at two fixed values of $t_\perp$ (t_2), i.e., two vertical and two horizontal line slices in the phase diagram of Fig. 2(c) which cross all the phases discovered. As can be seen, in the insulating phase located at the region where both $t_\perp$ and t_2 are weak, all double occupancies are suppressed to small values [MI region in Figs. 4(a) and 4(c)]. For this insulating phase, increasing either $t_\perp$ or t_2 will cause an increase in double occupancies on corresponding sites due to the formation of interlayer singlets there, whereas the double occupancies on the other sites remain nearly unchanged. This ultimately results in the emergence of two distinct insulating phases characterized by the coexistence of both small and large double occupancies
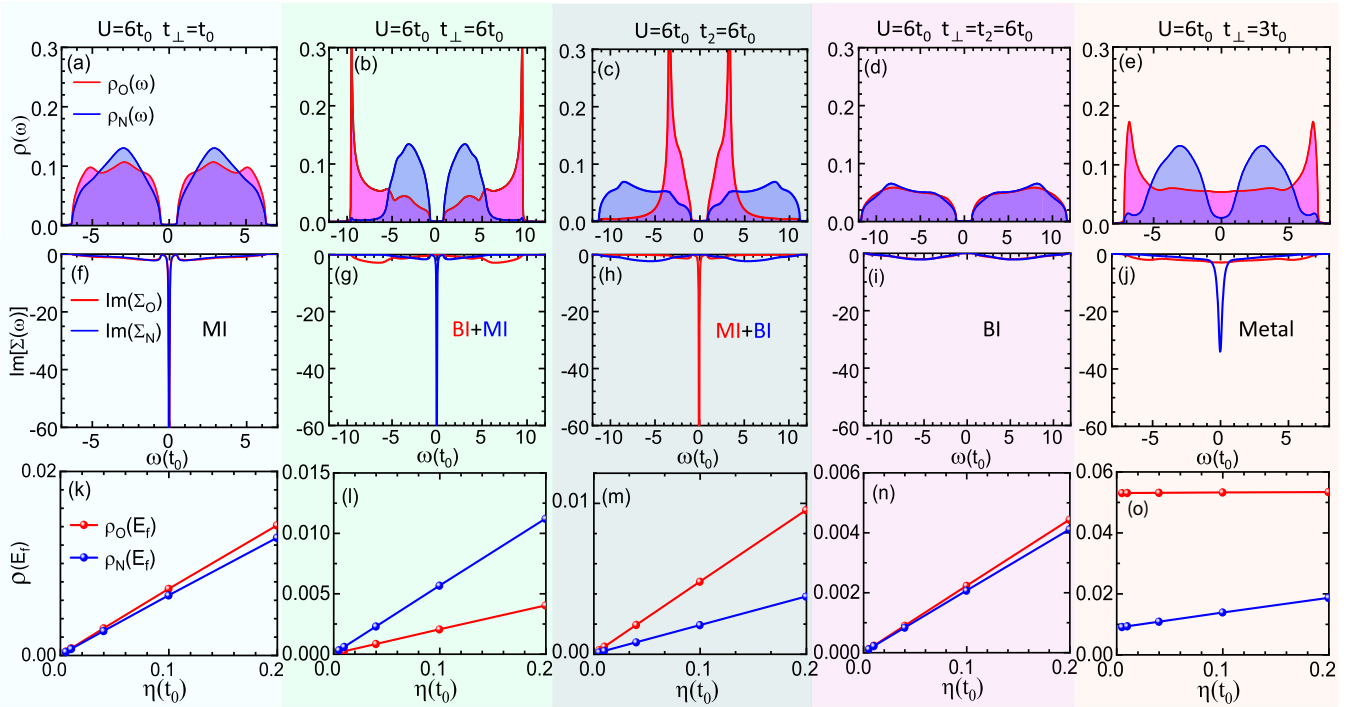
FIG. 5. The upper panel (a)–(e) depicts the DOS at various parameter points, where $\rho_O(\omega)$ (pink shadow) and $\rho_N(\omega)$ (blue shadow) represent the DOS at each site in regions O and N of the supercell, respectively. The middle panel (f)–(j) displays the imaginary part of self-energies under various parameter points, where $\text{Im}(\Sigma_O)$ (red line) and $\text{Im}(\Sigma_N)$ (blue line) describe the imaginary part of the self-energy at each site in regions O and N, respectively. The lower panel (k)–(o) shows the DOS at the Fermi level varied with the Lorentzian broadening factor η under various parameter points, where $\rho_O(E_f)$ (red line) and $\rho_N(E_f)$ (blue line) separately denote the DOS at the Fermi level of each site in regions O and N. Specifically, (a), (f), and (k) correspond to a Mott insulating phase, where $U = 6t_0$, $t_\perp = t_0$, and $t_1/t_0 = t_2/t_0 = 0$. (b),(g),(l) ($U = 6t_0$, $t_\perp = 6t_0$, and $t_1/t_0 = t_2/t_0 = 0$) as well as (c),(h),(m) ($U = 6t_0$, $t_2 = 6t_0$, and $t_1/t_0 = t_\perp/t_0 = 0$) depict two distinct site-selective insulating phases. Parts (d), (i), and (n) characterize a band insulating phase when $U = 6t_0$, $t_2 = t_\perp = 6t_0$, and $t_1/t_0 = 0$. Parts (e), (j), and (o) describe a metallic phase under the parameters of $U = 6t_0$, $t_\perp = 3t_0$, and $t_1/t_0 = t_2/t_0 = 0$. A Lorentzian broadening factor of $\eta = 0.01t_0$ is used in the upper and middle panels. As the MI+BI and BI in the t_1/t_0-$t_\perp/t_0$ plane are the same as those in the t_2/t_0-$t_\perp/t_0$ plane, we only present the corresponding physical quantities for the MI+BI and BI in the latter here.

[BI+MI region in Fig. 4(a) and MI+BI region in Fig. 4(c)]. Besides, all double occupancies exhibit relatively large values in the insulating phase where both $t_\perp$ and t_2 are strong [BI region in Figs. 4(b) and 4(d)]. Therefore, based on the behavior of the band gap and double occupancy, four distinct insulating phases are identified.

To clarify the natures of the aforementioned four insulating phases, we select one parameter point within each insulating phase [the parameter points are indicated above Figs. 5(a)–5(d), where the unspecified parameters are all set to 0] to calculate the corresponding DOS, the imaginary part of the self-energy, and the Lorentzian broadening factor η dependence of DOS at the Fermi level, as shown in Fig. 5, where the imaginary part of the self-energy is used to identify the Mott and band insulating states, while the DOS serves to distinguish the insulating phases from a metallic phase. Obviously, the opening of the band gap within the DOS in Figs. 5(a)–5(d) and the disappearance of both $\rho_O(E_f)$ and $\rho_N(E_f)$ as η approaches zero in Figs. 5(k)–5(n) further confirm the insulating behaviors of these phases.

We now focus on the imaginary part of their self-energies. It is apparent from Fig. 5(f) that both $\text{Im}(\Sigma_O)$ and $\text{Im}(\Sigma_N)$ diverge in proximity to zero frequency, which is a typical character of a Mott insulating phase [15,73]. In contrast, both

$\text{Im}(\Sigma_O)$ and $\text{Im}(\Sigma_N)$ vanish at $\omega = 0$ in Fig. 5(i), clearly indicating the occurrence of a band insulating phase. Surprisingly, $\text{Im}(\Sigma_O)$ and $\text{Im}(\Sigma_N)$ exhibit distinct behaviors at zero frequency for both Figs. 5(g) and 5(h), where $\text{Im}(\Sigma_N)$ diverges but $\text{Im}(\Sigma_O)$ vanishes in Fig. 5(g) while $\text{Im}(\Sigma_N)$ vanishes but $\text{Im}(\Sigma_O)$ diverges in Fig. 5(h), suggesting the presence of two distinct site-selective phases with the coexistence of band and Mott insulating states in the system.

For comparison, we also calculate the same physical quantities for a metallic phase. Apparently, the closure of the gap in the DOS [Fig. 5(e)] and the finite values of both $\rho_O(E_f)$ and $\rho_N(E_f)$ as η approaches zero [Fig. 5(o)] are key features of a metallic phase. It is necessary to mention that the nonzero imaginary part of the self-energy at $\omega = 0$ [Fig. 5(j)] is attributed to the failure of the CPA to reproduce a Fermi-liquid state [74]. However, this does not affect its conclusion regarding the metallic phase. Therefore, by conducting comprehensive analyses of the band gap, double occupancy, DOS, the imaginary part of the self-energies, as well as the Lorentzian broadening factor dependence of DOS at the Fermi level, we distinguish a Mott insulating phase, a band insulating phase, two distinct site-selective phases, and a metallic phase within the paramagnetic phase diagrams of this twisted system, which have been summarized in Fig. 2.
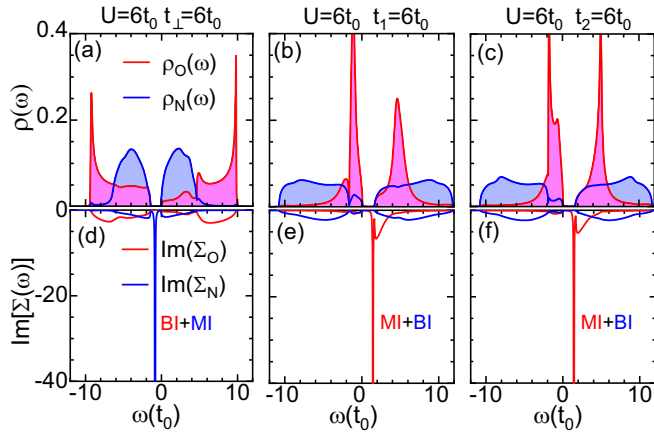
FIG. 6. The upper panel (a)–(c) illustrates the DOS at various parameter points, where $\rho_O(\omega)$ (pink shadow) and $\rho_N(\omega)$ (blue shadow) denote the DOS at each site in region O and region N of the supercell, respectively. The lower panel (d)–(f) presents the imaginary part of self-energies at various parameter points, where $Im(\Sigma_O)$ (red line) and $Im(\Sigma_N)$ (blue line) describe separately the imaginary part of the self-energy at each site in region O and region N. Parts (a) and (d) adopt the parameters of $U = 6t_0$, $t_\perp = 6t_0$, $t_1/t_0 = t_2/t_0 = 0$, and $\Delta_O - \Delta_N = 1.25t_0$. $U = 6t_0$, $t_1 = 6t_0$, $t_\perp/t_0 = t_2/t_0 = 0$, and $\Delta_O - \Delta_N = 1.25t_0$ are used in (b) and (e). $U = 6t_0, t_2 = 6t_0, t_\perp/t_0 = t_1/t_0 = 0$, and $\Delta_O - \Delta_N = 1.25t_0$ are employed in (c) and (f).

Finally, we will examine the effect of an on-site potential difference on the stability of the site-selective insulating phases. As we know, the Mott insulating state has already been pointed out to be unstable to the ionic potential in the ionic Hubbard model [75]. In the twisted system we studied, due to the emergence of two types of inequivalent sites, it also possesses two distinct on-site potentials including Δ_O and Δ_N, which are analogous to the ionic potentials. Thus, it is necessary to study whether the site-selective insulating phases (the Mott insulating state present at some sites) disappear as long as there is an on-site potential difference. In Fig. 6, we demonstrate the DOS and the imaginary part of the self-energy for the site-selective insulating phases (at three parameter points) under the effect of a moderate on-site potential difference with $\Delta_O - \Delta_N = 1.25t_0$. It is clear from Figs. 6(a)–6(c) that, although the on-site potential difference breaks the particle-hole symmetry, the band gap is still preserved, indicating the system in certain insulating phases. By further examining the imaginary parts of the self-energies of these insulating phases, we discover that $Im(\Sigma_N)$ in Fig. 6(d) as well as $Im(\Sigma_O)$ in both Figs. 6(e) and 6(f) exhibit a divergent behavior within the band gap at a nonzero frequency. It has been pointed out that this divergence means the infinite values of both the scattering rate and the effective mass of quasiparticles, namely the Mott physics at corresponding sites induced by strong electronic correlation [69]. Conversely, $Im(\Sigma_O)$ in Fig. 6(d) as well as $Im(\Sigma_N)$ in both Figs. 6(e) and 6(f) are negligibly small near the Fermi level, an indication of a band insulating state at related sites. Therefore, these two site-selective insulating phases are still stable even in the presence of a moderate on-site potential difference.

IV. DISCUSSION

In this paper, we have demonstrated the presence of site-selective insulating phases in the half-filled Hubbard model on a twisted bilayer square lattice using the CPA. While the CPA provides a critical on-site Coulomb interaction of $U_c \approx W/2 = 4t_0$ (W is the Bloch bandwidth) for the metal-Mott insulator transition in the monolayer square lattice, which differs slightly from other methods [39,72] (consistent with Ref. [71]), previous research indicates that the critical U_c is quite complicated and depends strongly on the Hubbard model under investigation and the methods employed [76]. Regardless of the specific critical phase transition point, the CPA remains a reliable approach capable of handling phase transitions among band insulating, Mott insulating, and metallic states [57–59,69,70]. Therefore, our discovery of the site-selective insulating phases is qualitatively reliable, as the site-selective insulating phases we found are merely composed of a band insulating state and a Mott insulating state. Noticeably, the CPA ignores the spatial fluctuations of the effective medium (the self-energy is momentum-independent), and it is interesting to employ other methods like CDMFT [77] to precisely determine the detailed phase boundaries when taking into account the effects of short-range spatial correlations.

As we know, as long as a weak on-site Coulomb interaction is present, an antiferromagnetic insulating phase emerges in the region of weak interlayer hopping within the magnetic phase diagram for the Hubbard model on an untwisted bilayer square lattice, which is attributed to the perfect nesting property of the Fermi surface within the noninteracting system [38,39]. However, when the twist is employed between two layers, the perfect nesting property of the Fermi surface is destroyed by the hoppings between two relatively twisted layers, which may have a significant impact on its phase diagram. In addition, we observe the site-selective phases even in the paramagnetic phase diagrams. Therefore, it is foreseeable that there will be various fascinating phases in the magnetic phase diagram of twisted bilayer square lattices.

Twist and pressure can manipulate interlayer hoppings and thereby induce novel phases in the layered systems; for example, the interlayer ferromagnetic and interlayer antiferromagnetic states can coexist in bilayer CrI_3 when twisting two layers with an angle of $\theta \leqslant 3°$ [78], and the phase transition from a nonmagnetic state to a ferromagnetic state emerges in twisted bilayer graphene nanoflake when applying pressure perpendicular to the layers [79]. We have demonstrated that the site-selective phases depend on the detailed values of interlayer hoppings. Therefore, it is quite intriguing to consider whether more complicated site-selective phases exist at different twisted angles or if phase transitions from the site-selective insulating phases to other phases occur under pressure.

Our discovery of the site-selective insulating phases in a twisted bilayer square lattice suggests twist as an effective approach to access a site-selective phase in the strongly correlated system. While our proposal remains a theoretical prediction, it may still stimulate tremendous research interest

for the following reasons. First, one may be interested in exploring whether a site-selective superconducting phase, where certain sites exhibit a superconducting state while the others are in a normal state, exists in twisted layered superconducting materials since there are currently mature experimental techniques for synthesizing monolayer superconducting material [80,81] and constructing two superconducting crystals along the c axis with a twist (c-axis twisted Josephson junctions) [82–88]. Second, while we predict the site-selective phase in a square lattice, it is possible that a site-selective phase may also be present in twisted systems with other lattice structures, making it intriguing to explore a site-selective insulating phase with the coexistence of band and Mott insulating states in twisted layered strongly correlated materials, not limited to square lattice materials. Finally, the nature of the Mott insulator observed in magic-angle twisted bilayer graphene [1] is worth reexamining since the DOS of the flat bands is primarily contributed by the atoms located at the AA-stacking zone [89]. Considering that in the absence of Coulomb interactions, atoms in the AB-stacking zone lack electrons near the Fermi level, it is likely that this observed insulating phase (induced by the interaction) is a site-selective phase, where the atoms located at the AA-stacking zone exhibit a Mott insulating state while others maintain a band insulating state.

V. CONCLUSION

In conclusion, we systematically investigate the paramagnetic phase diagrams of the half-filled Hubbard model on a twisted bilayer square lattice by employing the CPA. The site-selective insulating phases are discovered, characterized by the coexistence of band insulating states at some sites and Mott insulating states at the remaining, in addition to the pure metallic, band insulating, and Mott insulating phases in the whole lattice. We attribute the appearance of site-selective insulating phases to the differentiation of interlayer hoppings in different regions with the help of strong on-site Coulomb repulsions. We find that the site-selective insulating phases are stable even in the presence of a moderate site-dependent on-site potential. Our findings not only demonstrate a fascinating phenomenon that a band insulating state can coexist with a Mott insulating state in strongly correlated systems, but they also suggest that varieties of site-selective phases might be realized by applying twist to layered materials.

APPENDIX: THE MAPPING OF MODELS FROM A DISORDERED ALLOY TO AN EFFECTIVE MEDIUM WITHIN THE FRAMEWORK OF THE CPA

To derive the mapping from model (3) to model (4) within the framework of the CPA, we start by calculating the single-particle Green's function of the effective medium. Based on model (4), the corresponding Hamiltonian of the effective medium in momentum space reads

$$H_{\text{eff}} = \sum_{k,\sigma} |\psi_{k,\sigma}\rangle \widehat{\mathcal{M}}(k) \langle\psi_{k,\sigma}|, \tag{A1}$$

where

$$\widehat{\mathcal{M}}(k) = \begin{bmatrix}
\Delta_{\text{O}}-\mu+\Sigma_{A1} & -t_0 & -t_0 e^{-ik_x} & -t_0 e^{-i(k_x+k_y)} & -t_0 e^{-ik_y} & -t_\perp & 0 & 0 & 0 & 0 \\
-t_0 & \Delta_{\text{N}}-\mu+\Sigma_{B1} & -t_0 & -t_0 e^{-ik_y} & -t_0 & 0 & -t_2 & 0 & 0 & -t_1 \\
-t_0 e^{ik_x} & -t_0 & \Delta_{\text{N}}-\mu+\Sigma_{C1} & -t_0 & -t_0 e^{ik_x} & 0 & 0 & 0 & -t_1 & -t_2 \\
-t_0 e^{i(k_x+k_y)} & -t_0 e^{ik_y} & -t_0 & \Delta_{\text{N}}-\mu+\Sigma_{D1} & -t_0 & 0 & 0 & -t_1 & -t_2 & 0 \\
-t_0 e^{ik_y} & -t_0 & -t_0 e^{-ik_x} & -t_0 & \Delta_{\text{N}}-\mu+\Sigma_{E1} & 0 & -t_1 & -t_2 & 0 & 0 \\
-t_\perp & 0 & 0 & 0 & 0 & \Delta_{\text{O}}-\mu+\Sigma_{A2} & -t_0 & -t_0 e^{-ik_y} & -t_0 e^{-i(k_x+k_y)} & -t_0 e^{-ik_x} \\
0 & -t_2 & 0 & 0 & -t_1 & -t_0 & \Delta_{\text{N}}-\mu+\Sigma_{B2} & -t_0 & -t_0 e^{-ik_x} & -t_0 \\
0 & 0 & 0 & -t_1 & -t_2 & -t_0 e^{ik_y} & -t_0 & \Delta_{\text{N}}-\mu+\Sigma_{C2} & -t_0 & -t_0 e^{ik_y} \\
0 & 0 & -t_1 & -t_2 & 0 & -t_0 e^{i(k_x+k_y)} & -t_0 e^{ik_x} & -t_0 & \Delta_{\text{N}}-\mu+\Sigma_{D2} & -t_0 \\
0 & -t_1 & -t_2 & 0 & 0 & -t_0 e^{ik_x} & -t_0 & -t_0 e^{-ik_y} & -t_0 & \Delta_{\text{N}}-\mu+\Sigma_{E2}
\end{bmatrix} \tag{A2}$$

and

$$|\psi_{k,\sigma}\rangle = (C^\dagger_{kA1\sigma}, \quad C^\dagger_{kB1\sigma}, \quad C^\dagger_{kC1\sigma}, \quad C^\dagger_{kD1\sigma}, \quad C^\dagger_{kE1\sigma}, \quad C^\dagger_{kA2\sigma}, \quad C^\dagger_{kB2\sigma}, \quad C^\dagger_{kC2\sigma}, \quad C^\dagger_{kD2\sigma}, \quad C^\dagger_{kE2\sigma}). \tag{A3}$$

Here, all of these self-energies $\Sigma_{A1}, \ldots, \Sigma_{E2}$ are both complex and energy-dependent. Noticeably, the Hamiltonian matrix $\widehat{\mathcal{M}}(k)$ omits the spin indices as we are interested in the paramagnetic phase. Thus, the Green's function of the effective medium in momentum space can be readily calculated as

$$G^{\text{eff}}(k, \omega) = \frac{1}{\omega - \widehat{\mathcal{M}}(k) + i\eta}, \tag{A4}$$

where η stands for the Lorentzian broadening factor. Using the Green's function in momentum space, the corresponding Green's function of the effective medium in real space reads

$$G_{ism,ism}^{\text{eff}}(\omega) = \frac{1}{\Omega_{\text{BZ}}} \int_{\Omega_{\text{BZ}}} G_{sm,sm}^{\text{eff}}(\boldsymbol{k}, \omega) d\boldsymbol{k}, \qquad \text{(A5)}$$

where the integral is over the first Brillouin zone of the system. Then, the cavity Green's function $\mathcal{G}_{ism}(\omega)$ can be obtained through the Dyson equation

$$\mathcal{G}_{ism}^{-1}(\omega) = \left[G_{ism,ism}^{\text{eff}}(\omega) \right]^{-1} + \Sigma_{sm}(\omega) \qquad \text{(A6)}$$

for a given s sublattice at the m layer of the ith supercell, which describes a medium with removed self-energy at a chosen site. It is necessary to mention that the self-energies of the effective medium arise from the disordered potentials of the disordered alloy within the framework of the CPA, suggesting that the cavity Green's function for a given site of the effective medium is equal to that of the disordered alloy. Therefore, the cavity can now be filled by a real "impurity" with disorder potential, resulting in an impurity Green's function of the disordered alloy

$$G_{ism}(\omega) = \frac{1}{\mathcal{G}_{ism}^{-1}(\omega) - E_{ism}} \qquad \text{(A7)}$$

with impurity configurations of

$$\begin{aligned} E_{ism} &= 0, \quad P_0 = 1 - \langle n_{ism\bar{\sigma}} \rangle, \\ E_{ism} &= U, \quad P_U = \langle n_{ism\sigma} \rangle. \end{aligned} \qquad \text{(A8)}$$

Then, the average Green's function of the disordered alloy can be calculated by summing all the impurity Green's functions with corresponding probability weights, namely

$$\langle G_{ism}(\omega) \rangle = \frac{P_0}{\mathcal{G}_{ism}^{-1}(\omega) - 0} + \frac{P_U}{\mathcal{G}_{ism}^{-1}(\omega) - U}. \qquad \text{(A9)}$$

Once the average Green's function of the disordered alloy and the Green's function of the effective medium satisfies

$$\langle G_{ism}(\omega) \rangle = G_{ism,ism}^{\text{eff}}(\omega), \qquad \text{(A10)}$$

the model (3) can be successfully mapped into model (4). Noticeably, since we focus on the case at half-filling, the extra condition must be satisfied,

$$\sum_{sm} \langle n_{ism\sigma} \rangle = 5, \qquad \text{(A11)}$$

where

$$\langle n_{ism\sigma} \rangle = -\frac{1}{\pi} \int_{-\infty}^{0} \text{Im} \left[G_{ism,ism}^{\text{eff}}(\omega) \right] d\omega. \qquad \text{(A12)}$$

These calculated average occupation numbers need to be applied to compute the new probability of impurities (A8).

[1] Y. Cao, V. Fatemi, A. Demir, S. Fang, S. L. Tomarken, J. Y. Luo, J. D. Sanchez-Yamagishi, K. Watanabe, T. Taniguchi, E. Kaxiras *et al.*, Correlated insulator behaviour at half-filling in magic-angle graphene superlattices, Nature (London) **556**, 80 (2018).

[2] G. Chen, L. Jiang, S. Wu, B. Lyu, H. Li, B. L. Chittari, K. Watanabe, T. Taniguchi, Z. Shi, J. Jung *et al.*, Evidence of a gate-tunable Mott insulator in a trilayer graphene moiré superlattice, Nat. Phys. **15**, 237 (2019).

[3] E. C. Regan, D. Wang, C. Jin, M. I. Bakti Utama, B. Gao, X. Wei, S. Zhao, W. Zhao, Z. Zhang, K. Yumigeta *et al.*, Mott and generalized Wigner crystal states in WSe₂/WS₂ moiré superlattices, Nature (London) **579**, 359 (2020).

[4] Y. Tang, L. Li, T. Li, Y. Xu, S. Liu, K. Barmak, K. Watanabe, T. Taniguchi, A. H. MacDonald, J. Shan *et al.*, Simulation of Hubbard model physics in WSe₂/WS₂ moiré superlattices, Nature (London) **579**, 353 (2020).

[5] T. Li, S. Jiang, L. Li, Y. Zhang, K. Kang, J. Zhu, K. Watanabe, T. Taniguchi, D. Chowdhury, L. Fu *et al.*, Continuous Mott transition in semiconductor moiré superlattices, Nature (London) **597**, 350 (2021).

[6] Y. Cao, V. Fatemi, S. Fang, K. Watanabe, T. Taniguchi, E. Kaxiras, and P. Jarillo-Herrero, Unconventional superconductivity in magic-angle graphene superlattices, Nature (London) **556**, 43 (2018).

[7] G. Chen, A. L. Sharpe, P. Gallagher, I. T. Rosen, E. J. Fox, L. Jiang, B. Lyu, H. Li, K. Watanabe, T. Taniguchi *et al.*, Signatures of tunable superconductivity in a trilayer graphene moiré superlattice, Nature (London) **572**, 215 (2019).

[8] M. J. Park, Y. Kim, G. Y. Cho, and S. B. Lee, Higher-order topological insulator in twisted bilayer graphene, Phys. Rev. Lett. **123**, 216803 (2019).

[9] O. Can, T. Tummuru, R. P. Day, I. Elfimov, A. Damascelli, and M. Franz, High-temperature topological superconductivity in twisted double-layer copper oxides, Nat. Phys. **17**, 519 (2021).

[10] P. M. Eugenio and O. Vafek, Twisted-bilayer FeSe and the Fe-based superlattices, SciPost Phys. **15**, 081 (2023).

[11] J. Hubbard, Electron correlations in narrow energy bands III. An improved solution, Proc. R. Soc. London A **281**, 401 (1964).

[12] A. Koga, N. Kawakami, T. M. Rice, and M. Sigrist, Orbital-selective Mott transitions in the degenerate Hubbard model, Phys. Rev. Lett. **92**, 216402 (2004).

[13] L. deMedici, S. R. Hassan, M. Capone, and X. Dai, Orbital-selective Mott transition out of band degeneracy lifting, Phys. Rev. Lett. **102**, 126401 (2009).

[14] P. Werner and A. J. Millis, High-spin to low-spin and orbital polarization transitions in multiorbital Mott systems, Phys. Rev. Lett. **99**, 126405 (2007).

[15] Z.-Y. Song, H. Lee, and Y.-Z. Zhang, Possible origin of orbital selective Mott transitions in iron-based superconductors and Ca₂₋ₓSrₓRuO₄, New J. Phys. **17**, 033034 (2015).

[16] Y. Z. Zhang, Dimerization in a half-filled one-dimensional extended Hubbard model, Phys. Rev. Lett. **92**, 246404 (2004).

[17] S. S. Kancharla and E. Dagotto, Correlated insulated phase suggests bond order between band and Mott insulators in two dimensions, Phys. Rev. Lett. **98**, 016402 (2007).

[18] H. J. Schulz, Superconductivity and antiferromagnetism in the two-dimensional Hubbard model: Scaling theory, Europhys. Lett. **4**, 609 (1987).

[19] Th. A. Maier, M. Jarrell, T. C. Schulthess, P. R. C. Kent, and J. B. White, Systematic study of d-wave superconductivity in the 2D repulsive Hubbard model, Phys. Rev. Lett. **95**, 237001 (2005).

[20] T. Ogawa, K. Kanda, and T. Matsubara, Gutzwiller approximation for antiferromagnetism in Hubbard model, Prog. Theor. Phys. **53**, 614 (1975).

[21] H. J. Schulz, Incommensurate antiferromagnetism in the two-dimensional Hubbard model, Phys. Rev. Lett. **64**, 1445 (1990).

[22] J. E. Hirsch and S. Tang, Antiferromagnetism in the two-dimensional Hubbard model, Phys. Rev. Lett. **62**, 591 (1989).

[23] F. Wu, T. Lovorn, E. Tutuc, and A. H. MacDonald, Hubbard model physics in transition metal dichalcogenide moiré bands, Phys. Rev. Lett. **121**, 026402 (2018).

[24] H. Pan, F. Wu, and S. D. Sarma, Band topology, Hubbard model, Heisenberg model, and Dzyaloshinskii-Moriya interaction in twisted bilayer WSe$_2$, Phys. Rev. Res. **2**, 033087 (2020).

[25] H. Pan, F. Wu, and S. D. Sarma, Quantum phase diagram of a Moiré-Hubbard model, Phys. Rev. B **102**, 201104(R) (2020).

[26] A. Wietek, J. Wang, J. Zang, J. Cano, A. Georges, and A. Millis, Tunable stripe order and weak superconductivity in the Moiré Hubbard model, Phys. Rev. Res. **4**, 043048 (2022).

[27] N. Morales-Durán, N. C. Hu, P. Potasz, and A. H. MacDonald, Nonlocal interactions in moiré hubbard systems, Phys. Rev. Lett. **128**, 217202 (2022).

[28] T. Huang, L. Zhang, and T. Ma, Antiferromagnetically ordered mott insulator and $d + id$ superconductivity in twisted bilayer graphene: A quantum monte carlo study, Sci. Bull. **64**, 310 (2019).

[29] X. Lu and D. Sénéchal, Doping phase diagram of a Hubbard model for twisted bilayer cuprates, Phys. Rev. B **105**, 245127 (2022).

[30] M. Bélanger and D. Sénéchal, Doping dependence of chiral superconductivity in near 45° twisted bilayer cuprates, Phys. Rev. B **109**, 045111 (2024).

[31] D. Fournier, G. Levy, Y. Pennec, J. L. McChesney, A. Bostwick, E. Rotenberg, R. Liang, W. N. Hardy, D. A. Bonn, I. S. Elfimov *et al.*, Loss of nodal quasiparticle integrity in underdoped YBa$_2$Cu$_3$O$_{6+x}$, Nat. Phys. **6**, 905 (2010).

[32] M. Gall, N. Wurz, J. Samland, C. F. Chan, and M. Köhl, Competing magnetic orders in a bilayer Hubbard model with ultracold atoms, Nature (London) **589**, 40 (2021).

[33] R. T. Scalettar, J. W. Cannon, D. J. Scalapino, and R. L. Sugar, Magnetic and pairing correlations in coupled Hubbard planes, Phys. Rev. B **50**, 13419 (1994).

[34] A. Fuhrmann, D. Heilmann, and H. Monien, From Mott insulator to band insulator: A dynamical mean-field theory study, Phys. Rev. B **73**, 245118 (2006).

[35] S. S. Kancharla and S. Okamoto, Band insulator to Mott insulator transition in a bilayer Hubbard model, Phys. Rev. B **75**, 193103 (2007).

[36] K. Bouadim, G. G. Batrouni, F. Hébert, and R. T. Scalettar, Magnetic and transport properties of a coupled Hubbard bilayer with electron and hole doping, Phys. Rev. B **77**, 144527 (2008).

[37] Y. Mou, R. Mondaini, and R. T. Scalettar, Bilayer Hubbard model: Analysis based on the fermionic sign problem, Phys. Rev. B **106**, 125116 (2022).

[38] M. Golor, T. Reckling, L. Classen, M. M. Scherer, and S. Wessel, Ground-state phase diagram of the half-filled bilayer Hubbard model, Phys. Rev. B **90**, 195131 (2014).

[39] R. Rüger, L. F. Tocchio, R. Valentí, and C. Gros, The phase diagram of the square lattice bilayer Hubbard model: a variational Monte Carlo study, New J. Phys. **16**, 033010 (2014).

[40] N. Lanatà, P. Barone, and M. Fabrizio, Superconductivity in the doped bilayer Hubbard model, Phys. Rev. B **80**, 224524 (2009).

[41] H. Zhai, F. Wang, and D.-H. Lee, Antiferromagnetically driven electronic correlations in iron pnictides and cuprates, Phys. Rev. B **80**, 064517 (2009).

[42] T. A. Maier and D. J. Scalapino, Pair structure and the pairing interaction in a bilayer Hubbard model for unconventional superconductivity, Phys. Rev. B **84**, 180513(R) (2011).

[43] K. Matsumoto, D. Ogura, and K. Kuroki, Strongly enhanced superconductivity due to finite energy spin fluctuations induced by an incipient band: a flex study on the bilayer Hubbard model with vertical and diagonal interlayer hoppings, J. Phys. Soc. Jpn. **89**, 044709 (2020).

[44] D. Kato and K. Kuroki, Many-variable variational Monte Carlo study of superconductivity in two-band Hubbard models with an incipient band, Phys. Rev. Res. **2**, 023156 (2020).

[45] S. Karakuzu, S. Johnston, and T. A. Maier, Superconductivity in the bilayer Hubbard model: Two Fermi surfaces are better than one, Phys. Rev. B **104**, 245109 (2021).

[46] A. Iwano and Y. Yamaji, Superconductivity in Bilayer $t - t'$ Hubbard Models, J. Phys. Soc. Jpn. **91**, 094702 (2022).

[47] H. Lee, Y.-Z. Zhang, H. O. Jeschke, and R. Valentí, Competition between band and Mott insulators in the bilayer Hubbard model: A dynamical cluster approximation study, Phys. Rev. B **89**, 035139 (2014).

[48] T. I. Vanhala, J. E. Baarsma, M. O. J. Heikkinen, M. Troyer, A. Harju, and P. Törmä, Superfluidity and density order in a bilayer extended Hubbard model, Phys. Rev. B **91**, 144510 (2015).

[49] H. Park, A. J. Millis, and C. A. Marianetti, Site-selective Mott transition in rare-earth-element nickelates, Phys. Rev. Lett. **109**, 156402 (2012).

[50] Y. Shimizu, S. Aoyama, T. Jinno, M. Itoh, and Y. Ueda, Site-selective mott transition in a quasi-one-dimensional vanadate V$_6$O$_{13}$, Phys. Rev. Lett. **114**, 166403 (2015).

[51] X.-L. Yu, D.-Y. Liu, Y.-M. Quan, T. Jia, H.-Q. Lin, and L.-J. Zou, A site-selective antiferromagnetic ground state in layered pnictide-oxide BaTi$_2$As$_2$O, J. Appl. Phys. **115**, 17A924 (2014).

[52] J. Hubbard, Electron correlations in narrow energy bands, Proc. R. Soc. London A **276**, 238 (1963).

[53] P. Soven, Coherent-potential model of substitutional disordered alloys, Phys. Rev. **156**, 809 (1967).

[54] B. Velický, S. Kirkpatrick, and H. Ehrenreich, Single-site approximations in the electronic theory of simple binary alloys, Phys. Rev. **175**, 747 (1968).

[55] R. J. Elliott, J. A. Krumhansl, and P. L. Leath, The theory and properties of randomly disordered crystals and related physical systems, Rev. Mod. Phys. **46**, 465 (1974).

[56] F. Gebhard, *The Mott Metal-Insulator Transition* (Springer, 1997).

[57] A. T. Hoang, Metal–insulator transitions in the half-filled ionic Hubbard model, J. Phys.: Condens. Matter **22**, 095602 (2010).

[58] D. A. Rowlands and Y.-Z. Zhang, Inclusion of intersite spatial correlations in the alloy analogy approach to the half-filled ionic Hubbard model, J. Phys.: Condens. Matter **26**, 274201 (2014).

[59] D. A. Rowlands and Y.-Z. Zhang, Disappearance of the Dirac cone in silicene due to the presence of an electric field, Chin. Phys. B **23**, 037101 (2014).

[60] F. F. Assaad and I. F. Herbut, Pinning the order: the nature of quantum criticality in the Hubbard model on honeycomb lattice, Phys. Rev. X **3**, 031010 (2013).

[61] S. Sorella, Y. Otsuka, and S. Yunoki, Absence of a spin liquid phase in the Hubbard model on the honeycomb lattice, Sci. Rep. **2**, 992 (2012).

[62] F. P. Toldin, M. Hohenadler, F. F. Assaad, and I. F. Herbut, Fermionic quantum criticality in honeycomb and π-flux Hubbard models: Finite-size scaling of renormalization-group-invariant observables from quantum Monte Carlo, Phys. Rev. B **91**, 165108 (2015).

[63] W. Wu, Y.-H. Chen, H.-S. Tao, N.-H. Tong, and W.-M. Liu, Interacting Dirac fermions on honeycomb lattice, Phys. Rev. B **82**, 245102 (2010).

[64] A. Liebsch, Correlated Dirac fermions on the honeycomb lattice studied within cluster dynamical mean field theory, Phys. Rev. B **83**, 035113 (2011).

[65] K. F. Mak, C. H. Lui, J. Shan, and T. F. Heinz, Observation of an electric-field-induced band gap in bilayer graphene by infrared spectroscopy, Phys. Rev. Lett. **102**, 256405 (2009).

[66] R T. Weitz, M. T. Allen, B. E. Feldman, J. Martin, and A. Yacoby, Broken-symmetry states in doubly gated suspended bilayer graphene, Science **330**, 812 (2010).

[67] B. Hunt, J. D. Sanchez-Yamagishi, A. F. Young, M. Yankowitz, B. J. LeRoy, K. Watanabe, T. Taniguchi, P. Moon, M. Koshino, P. Jarillo-Herrero *et al.*, Massive Dirac fermions and Hofstadter butterfly in a van der Waals heterostructure, Science **340**, 1427 (2013).

[68] Z.-G. Chen, Z. Shi, W. Yang, X. Lu, Y. Lai, H. Yan, F. Wang, G. Zhang, and Z. Li, Observation of an intrinsic bandgap and Landau level renormalization in graphene/boron-nitride heterostructures, Nat. Commun. **5**, 4461 (2014).

[69] J.-R. Xu, Z.-Y. Song, H.-Q. Lin, and Y.-Z. Zhang, Gate-induced gap in bilayer graphene suppressed by Coulomb repulsion, Phys. Rev. B **93**, 035109 (2016).

[70] J.-R. Xu, Z.-Y. Song, C.-G. Yuan, and Y.-Z. Zhang, Interaction-induced metallic state in graphene on hexagonal boron nitride, Phys. Rev. B **94**, 195103 (2016).

[71] C. Groeber, M. G. Zacher, and R. Eder, Paramagnetic metal-insulator transition in the 2D Hubbard model, arXiv:cond-mat/9810246.

[72] E. Gull, O. Parcollet, and A. J. Millis, Superconductivity and the pseudogap in the two-dimensional Hubbard model, Phys. Rev. Lett. **110**, 216405 (2013).

[73] Z.-Y. Song, X.-C. Jiang, H.-Q. Lin, and Y.-Z. Zhang, Distinct nature of orbital-selective Mott phases dominated by low-energy local spin fluctuations, Phys. Rev. B **96**, 235119 (2017).

[74] Y. Kakehashi and P. Fulde, Coherent potential approximation and projection operators for interacting electrons, Phys. Rev. B **69**, 045101 (2004).

[75] A. Garg, H. R. Krishnamurthy, and M. Randeria, Can correlations drive a band insulator metallic? Phys. Rev. Lett. **97**, 046403 (2006).

[76] H.-G. Luo and S.-J. Wang, Higher-order correlation effects to the solution of the Hubbard model, Phys. Rev. B **61**, 5158 (2000).

[77] G. Kotliar, S. Y. Savrasov, G. Pálsson, and G. Biroli, Cellular dynamical mean field approach to strongly correlated systems, Phys. Rev. Lett. **87**, 186401 (2001).

[78] Y. Xu, A. Ray, Y.-T. Shao, S. Jiang, K. Lee, D. Weber, J. E. Goldberger, K. Watanabe, T. Taniguchi, D. A. Muller *et al.*, Coexisting ferromagnetic–antiferromagnetic state in twisted bilayer CrI_3, Nat. Nanotechnol. **17**, 143 (2022).

[79] D. Pant and R. Pati, Phase transition from a nonmagnetic to a ferromagnetic state in a twisted bilayer graphene nanoflake: The role of electronic pressure on the magic-twist, Nanoscale **14**, 11945 (2022).

[80] Y. Yu, L. Ma, P. Cai, R. Zhong, C. Ye, J. Shen, G. D. Gu, X. H. Chen, and Y. Zhang, High-temperature superconductivity in monolayer $Bi_2Sr_2CaCu_2O_{8+\delta}$, Nature (London) **575**, 156 (2019).

[81] S. Y. F. Zhao, N. Poccia, M. G. Panetta, C. Yu, J. W. Johnson, H. Yoo, R. Zhong, G. D. Gu, K. Watanabe, T. Taniguchi *et al.*, Sign-reversing Hall effect in atomically thin high-temperature $Bi_{2.1}Sr_{1.9}CaCu_2O_{8+\delta}$ superconductors, Phys. Rev. Lett. **122**, 247001 (2019).

[82] Q. Li, Y. N. Tsay, M. Suenaga, R. A. Klemm, G. D. Gu, and N. Koshizuka, $Bi_2Sr_2CaCu_2O_{8+\delta}$ bicrystal C-axis twist Josephson junctions: a new phase-sensitive test of order parameter symmetry, Phys. Rev. Lett. **83**, 4160 (1999).

[83] Y. Takano, T. Hatano, A. Fukuyo, A. Ishii, M. Ohmori, S. Arisawa, K. Togano, and M. Tachiki, *d*-like symmetry of the order parameter and intrinsic Josephson effects in $Bi_2Sr_2CaCu_2O_{8+\delta}$ cross-whisker junctions, Phys. Rev. B **65**, 140513(R) (2002).

[84] Y. I. Latyshev, A. P. Orlov, A. M. Nikitina, P. Monceau, and R. A. Klemm, *c*-axis transport in naturally grown $Bi_2Sr_2CaCu_2O_{8+\delta}$ cross-whisker junctions, Phys. Rev. B **70**, 094517 (2004).

[85] Z. Yang, S. Qin, Q. Zhang, C. Fang, and J. Hu, $\pi/2$-Josephson junction as a topological superconductor, Phys. Rev. B **98**, 104515 (2018).

[86] Y. Zhu, M. Liao, Q. Zhang, H.-Y. Xie, F. Meng, Y. Liu, Z. Bai, S. Ji, J. Zhang, K. Jiang *et al.*, Presence of s-wave pairing in Josephson junctions made of twisted ultrathin $Bi_2Sr_2CaCu_2O_{8+x}$ flakes, Phys. Rev. X **11**, 031011 (2021).

[87] S. Y. Zhao, N. Poccia, X. Cui, P. A. Volkov, H. Yoo, R. Engelke, Y. Ronen, R. Zhong, G. Gu, S. Plugge *et al.*, Emergent interfacial superconductivity between twisted cuprate superconductors, arXiv:2108.13455.

[88] J. Lee, W. Lee, G.-Y. Kim, Y.-B. Choi, J. Park, S. Jang, G. Gu, S.-Y. Choi, G. Y. Cho, G.-H. Lee *et al.*, Twisted van der waals josephson junction based on a high-tc superconductor, Nano Lett. **21**, 10469 (2021).

[89] G. T. de Laissardière, D. Mayou, and L. Magaud, Localization of Dirac electrons in rotated graphene bilayers, Nano Lett. **10**, 804 (2010).